nature communications

Article

https://doi.org/10.1038/s41467-024-53324-z

# Spin-orbit proximity in $MoS_2$/bilayer graphene heterostructures

Received: 14 July 2024

Accepted: 7 October 2024

Published online: 26 October 2024

Check for updates

Michele Masseroni[1] ✉, Mario Gull[1], Archisman Panigrahi[2], Nils Jacobsen[3], Felix Fischer[1], Chuyao Tong[1], Jonas D. Gerber[1], Markus Niese[1], Takashi Taniguchi[4], Kenji Watanabe[5], Leonid Levitov[2], Thomas Ihn[1], Klaus Ensslin[1] ✉ & Hadrien Duprez[1]

Van der Waals heterostructures provide a versatile platform for tailoring electronic properties through the integration of two-dimensional materials. Among these combinations, the interaction between bilayer graphene and transition metal dichalcogenides (TMDs) stands out due to its potential for inducing spin–orbit coupling (SOC) in graphene. Future devices concepts require the understanding of the precise nature of SOC in TMD/bilayer graphene heterostructures and its influence on electronic transport phenomena. Here, we experimentally confirm the presence of two distinct types of SOC – Ising ($\Delta_I$ = 1.55 meV) and Rashba ($\Delta_R$ = 2.5 meV) – in bilayer graphene when interfaced with molybdenum disulfide. Furthermore, we reveal a non-monotonic trend in conductivity with respect to the electric displacement field at charge neutrality. This phenomenon is ascribed to the existence of single-particle gaps induced by the Ising SOC, which can be closed by a critical displacement field. Our findings also unveil sharp peaks in the magneto-conductivity around the critical displacement field, challenging existing theoretical models.

Spin is emerging as a promising alternative or complement to charge for information storage and processing[1]. Spin–orbit coupling (SOC) is crucial in spin-based devices, enabling manipulation of spin states through time-dependent electric fields[2,3]. Bernal bilayer graphene (BLG) holds potential for spintronics[4] and quantum computing[5], with recent studies indicating long spin relaxation times in BLG quantum dots[6–8]. However, intrinsic Kane–Mele (KM) SOC[9] in graphene is weak (40–80 μeV)[10,11]. Various methods have been explored to enhance SOC in BLG, including interfacing with high-SOC substrates. Transition metal dichalcogenides (TMDs) have shown promise in this regard, offering significant SOC enhancements (from 1 to 10 meV) without compromising graphene's electronic quality[12–14]. Additionally, the combination of BLG on $WSe_2$ has recently been shown to host an unexpected superconducting phase, where the SOC seems to play a major role[15,16], prompting further study of such heterostructures.

The extrinsic SOC induced in BLG by the TMDs is described by the Hamiltonian[17]

$$H_{SO} = \frac{\Delta_I}{2}\xi s_z \mathbb{I}_\sigma + \frac{\Delta_R}{2}(\xi\sigma_x s_y - \sigma_y s_x), \quad (1)$$

where $\xi = \pm 1$ represents the valley index, $s_{x,y,z}$ denote spin Pauli matrices, $\sigma_{x,y}$ and $\mathbb{I}_\sigma$ are Pauli and unit matrices operating on the sublattice degree of freedom ($A_1$, $B_1$) within the layer in contact with the TMD (see schematic in Fig. 2e). The first term, known as the Ising SOC, acts similarly to an effective out-of-plane magnetic field with a valley-dependent sign. It lifts the four-fold spin and valley degeneracy at the $K$

[1]Solid State Physics Laboratory, ETH Zürich, 8093 Zürich, Switzerland. [2]Department of Physics, Massachusetts Institute of Technology, Cambridge, MA 02139, USA. [3]1st Physical Institute, Faculty of Physics, University of Göttingen, 37077 Göttingen, Germany. [4]Research Center for Materials Nanoarchitectonics, National Institute for Materials Science, 1-1 Namiki, Tsukuba 305-0044, Japan. [5]Research Center for Electronic and Optical Materials, National Institute for Materials Science, 1-1 Namiki, Tsukuba 305-0044, Japan. ✉e-mail: masmiche@phys.ethz.ch; ensslin@phys.ethz.ch

± points, forming spin-valley-locked Kramers doublets. The second term is a Rashba type of SOC[18], favoring an in-plane spin polarization perpendicular to the sublattice isospin vector.

Intensive theoretical[17,19–23] and experimental efforts[12–14,24–28] in understanding and quantifying SOC proximity effects have led to a range of values for the relative strength of the two SOC terms depending on the analysis method. This is because the strength of SOC is often inferred indirectly, for example, through the extraction of relaxation times obtained from quantum interference effects such as weak antilocalization (WAL)[29–31], or spin precession measurements[32]. In contrast, the fundamental frequency $f = \Delta(B^{-1})$ of the Shubnikov–de Haas oscillations (SdHOs) offers a direct measurement of the Fermi surface and is suitable for determining the band splitting induced by SOC[33]. However, the energy resolution of this technique is limited by the broadening of the Landau levels, necessitating high electron mobilities and low disorder potentials.

Here, we conduct magnetotransport experiments on a dual-gated $MoS_2$/BLG heterostructure. First, we analyze SdHOs to quantify proximity-induced SOC. Our results confirm the presence of both Ising ($\Delta_I = 1.55$ meV) and Rashba ($\Delta_R = 2.5$ meV) SOC. Despite their comparable strength, we show that the splitting of the low-energy bands mainly arises from the Ising SOC. Additionally, we observe a non-monotonic conductivity response to an applied displacement field when BLG is charge-neutral. Our tight-binding calculations show how the displacement field $D$ opposes the Ising SOC, closing single-particle gaps in the spin-polarized bands at a critical value of $D_c$ and causing local maxima in the conductivity. In this critical field, the application of an external magnetic field rapidly suppresses the conductivity, challenging existing theoretical models and suggesting the involvement of many-body interactions.

## Results

### Proximity induced spin–orbit coupling

Determining the SOC gap in BLG via magnetotransport experiments is challenging due to disorder-induced density fluctuations $\delta n$. Shown in Fig. 1a is the schematic of our sample, comprising BLG atop three layers of $MoS_2$, encapsulated within hexagonal boron nitride (hBN), and placed on a graphite bottom gate. The use of hBN dielectrics and a graphite layer minimizes density fluctuations[34], evident from the low-density $\delta n \sim 2 \times 10^9$ cm$^{-2}$ at which conductivity saturates in our sample (Fig. 1b). High charge carrier mobilities [$\sim 5 \times 10^5$ cm$^2$ (V s)$^{-1}$ at $n = 5 \times 10^{10}$ cm$^{-2}$, see Supplementary Note 2] indicate minimal impact of the $MoS_2$ layer on BLG's electronic properties compared to hBN-encapsulated Bernal BLG devices[35].

We analyze SdHOs at zero displacement field ($D$) and low magnetic fields ($B$) to determine the band splitting induced by the SOC.

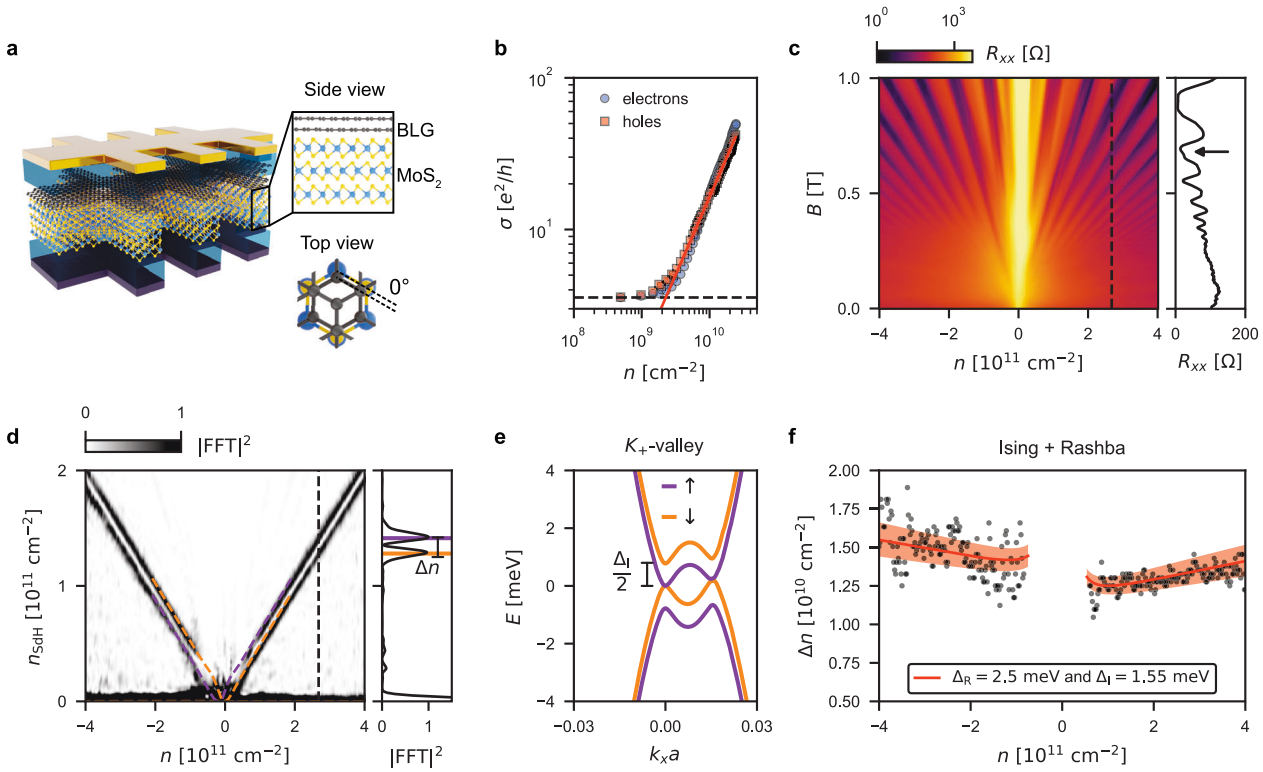


**Fig. 1 | Magnetotransport data at zero displacement field. a** Schematic representation of the BLG/$MoS_2$ heterostructure, illustrating a cross-section of the layers (top right panel) and highlighting the alignment of the BLG and $MoS_2$ layers (bottom right panel). **b** The conductivity is plotted as a function of carrier density on a logarithmic scale. The measurement was conducted at a temperature of approximately 30 mK. Dotted (squared) markers represent data for electron (hole) doping. The solid red line depicts a linear fit, while the black dashed line indicates the saturation of the conductivity. **c** Landau fan at zero displacement field (left panel) measured at a temperature $T = 1.3$ K. The right panel displays a vertical linecut at $n = 2.7 \times 10^{11}$ cm$^{-2}$ (dashed line in the left panel). **d** Fast Fourier transform (FFT) of the Landau fan shown in (**c**). The FFT of $R_{xx}(B^{-1})$ is calculated line-by-line for each density. The vertical axis has been rescaled according to $n_{SdH} = 2ef/h$, where $f$ is the frequency axis in Tesla, accounting for the valley degeneracy. Dashed lines represent densities obtained from the band structure in (**e**). The right panel shows a vertical linecut at $n = 2.7 \times 10^{11}$ cm$^{-2}$ (dashed line in the left panel). **e** Band structure of bilayer graphene with SOC ($\Delta_I = 1.55$ meV and $\Delta_R = 2.5$ meV) close to the $K_+$ point at zero displacement field. The bands are plotted along the relative momentum $k_x$ (or equivalently, along the line $\Gamma$–$K$–$M$ of the first Brillouin zone). The horizontal axis is scaled by the lattice constant $a = 2.46$ Å. The color of the bands encodes the spin texture (violet for spin up and orange for spin down). **f** Density difference $\Delta n$ obtained from the distance between the two peaks in the Fourier spectrum shown in (**d**). The red solid line represents a fit to the data, obtained from the band structure in (**e**) by determining the density of states and then the carrier densities $n_{\downarrow,\uparrow}$ followed by calculating the difference $|n_\downarrow - n_\uparrow|$. The fit yields the SOC parameters: $\Delta I = 1.55 \pm 0.10$ meV and $\Delta_R = 2.5 \pm 0.5$ meV. The shaded area indicates the uncertainty in the fitting parameters, reflected in the uncertainty in $\Delta n$.

https://doi.org/10.1038/s41467-024-53324-z

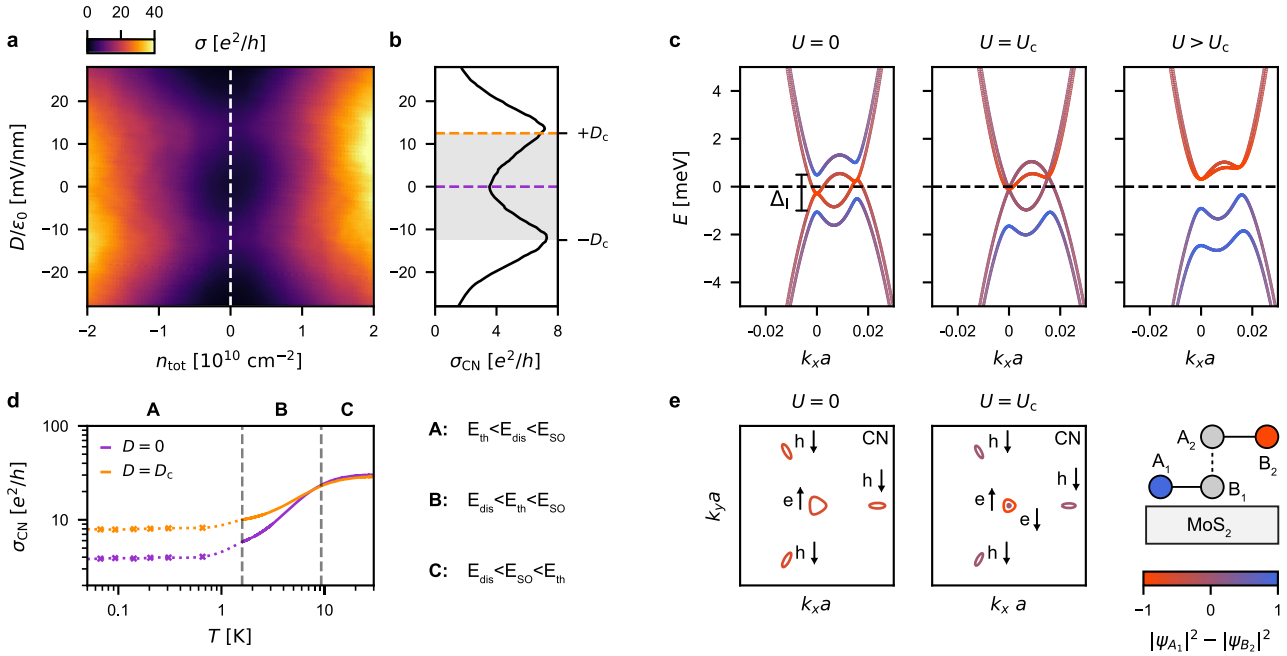


**Fig. 2 | Displacement field dependence of the conductivity at CN. a** Conductivity $\sigma$ as a function of density and displacement field measured at $T \approx 30$ mK. **b** Vertical line cut of $\sigma$ in (**a**) at CN. The conductivity shows local maxima at the critical displacement $D_c = \pm 12.5$ mV/nm. **c** Band structure of proximitized BLG at the $K$ point. The calculation includes an Ising SOC term with $\Delta_I = 1.55$ meV. The band structure is shown for three characteristic interlayer potential energies: $U = 0$ (left panel), $U = 0.775$ meV (central panel), and $U = 2$ meV (right panel). The energy axis is adjusted such that $E = 0$ corresponds to charge neutrality, which is marked by the horizontal dashed lines. The color code represents the layer polarization: blue indicates polarization on layer 1, while red is on layer 2, as shown in the schematics in the bottom right panel. The band structure shown in the left panel is the same as Fig. 1c, where we color-coded the bands according to the spin texture. **d** Conductivity at CN for $D = 0$ (violet) and $D = D_c$ (orange) as a function of temperature in logarithmic scale. The crosses were measured in a dilution refrigerator, while the solid line was measured in a pumped He4 cryostat. The temperature range is divided into three regimes (A–C), according to relevant energy scales ($E_{th}$, $E_{dis}$, $E_{SO}$) defined in the main text. **e** Constant energy contours of the Fermi energy at charge neutrality for $U = 0$ (left panel) and $U = U_c$ (right panel). The Fermi pockets are labeled according to their doping, electron e and holes h, and their spin (↑, ↓). Schematic: The side view of the BLG unit cell is schematically shown on a $MoS_2$ substrate. The color bar underneath defines the polarization of the electron wave function on the low energy orbitals, which are localized on the lattice site $A_1$ and $B_2$ (colored blue and red, respectively).

Figure 1c shows the longitudinal resistance $R_{xx}$ as a function of $B$ and electron density $n$ at $T = 1.3$ K. Pronounced minima in resistance $R_{xx}$ occur at filling factors $\nu = \pm 4N$ ($N$ an integer), characteristic of pristine BLG. In addition, small oscillation maxima appear in the SdH minima (highlighted by the arrow in the right panel), suggesting the presence of a broken symmetry.

To determine the oscillation frequency of the SdHOs, we employ a numerical fast Fourier transform (FFT) of $R_{xx}(1/B)$ calculated line-by-line for each density, as shown in Fig. 1d. The FFT reveals two clear frequencies $f_1$ and $f_2$, resulting from the splitting of the Fermi surface, which is attributed to the influence of the $MoS_2$ substrate through the spin–orbit proximity effect. The sum of the electron densities $n_i = 2ef_i/h$ ($i = 1, 2$) obtained from the SdHO matches the Hall density by accounting for the twofold valley degeneracy, as expected.

The two SOC terms in Eq. (1) yield distinct density dependencies for the spin–orbit splitting. The Ising SOC induces a constant splitting as a function of the Fermi energy (and hence density), while the Rashba term leads to a splitting that increases with the Fermi energy. Although the splitting in Fig. 1d initially appears constant with carrier density, a closer examination of $\Delta n$ in Fig. 1f reveals a small but detectable slope. By aligning the density difference $\Delta n$ obtained from the tight-binding model (see the "Methods" subsection "Tight-binding model" and Supplementary Notes 3–5) with the data (illustrated by the red solid line), we find $\Delta_I = (1.55 \pm 0.10)$ meV and $\Delta_R = (2.5 \pm 0.5)$ meV. The theoretically predicted densities with these parameters are overlaid against the total density in Fig. 1d as orange and violet dashed lines, demonstrating good agreement with the experimental data. We acknowledge that the numerical outcome of the fit can be subtly influenced by the choice of the tight-binding intralayer and interlayer coupling parameters of BLG, referred to as the Slonczewski–Weiss–McClure parameters. These parameters dictate the curvature of the bands, thereby affecting the conversion between energy and density, as elaborated in Supplementary Note 4.

We validate our findings at finite displacement fields, leveraging the layer-dependent SOC induced by the asymmetric structure of our sample[3]. This layer selectivity is demonstrated in Supplementary Note 6, where the electron wave function is polarized via the applied displacement field in one layer or the other, depending on its sign.

Next, we continue the discussion by investigating the impact of SOC on the electrical conductivity ($\sigma$) of BLG at charge neutrality (CN).

## Conductivity at charge neutrality

Measurements of $\sigma$ reveal a non-monotonic dependence on the displacement field (Fig. 2a), which appears in a narrow density range ($n \sim 1 \times 10^{10}$ cm$^{-2}$) around CN. A local minimum at $D = 0$ is surrounded by conductivity maxima at $D = \pm D_c \approx 12.5$ mV/nm, as highlighted in the line cut at $n = 0$ presented in Fig. 2b.

This dependence can be understood by taking into account the influence of SOC on the BLG band structure. From tight-binding calculations, we find that the Rashba SOC has little effect on the low-energy bands (see Supplementary Note 3 for more details). For this reason, we consider only the Ising SOC in the following discussion. The outcome of the band structure calculations is presented in Fig. 2c, shown for the $K_+$-valley and three characteristic interlayer potential energies ($U$). First, we consider the case $U = 0$ in the left panel. We observe that the band structure comprises two pairs of bands, one split

https://doi.org/10.1038/s41467-024-53324-z

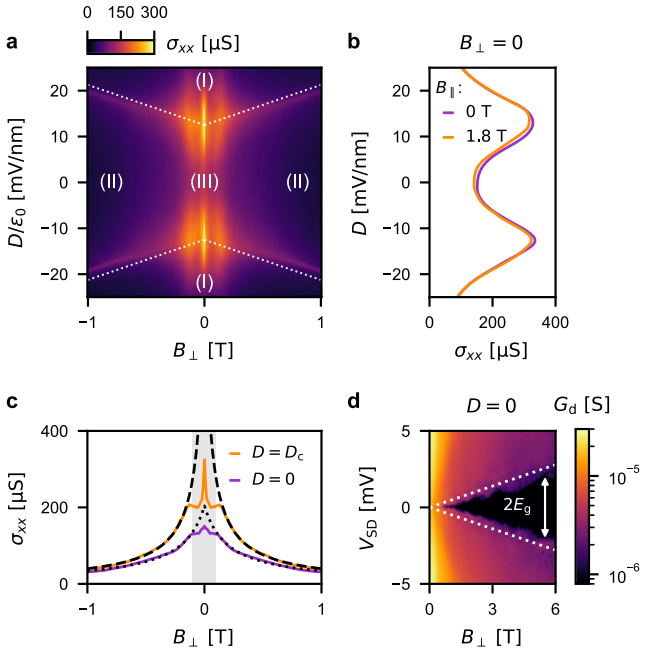


**Fig. 3 | Magnetotransport data at CN. a** Conductivity as a function of $B_\perp$ and $D$ at $T = 30$ mK. This plot represents the ($D$, $B$) phase diagram of SOC proximitized BLG. Phase (I) is a gapped phase with a layer-polarized wave function. Phase (II) is another gapped phase that has been attributed to the canted antiferromagnetic phase in pristine BLG[41,62]. The phase boundary between phases (I) and (II) (straight dotted lines) is described in Supplementary Note 10. Phase (III) is a weakly insulating phase that arises from the presence of spin-gaps in the single-particle spectrum. **b** $\sigma_{xx}$ plotted against $D$ for $B_\perp = 0$ and two values of in-plane magnetic field: $B_\parallel = 0$ (violet) and $B_\parallel = 1.8$ T (orange). **c** Linecuts of panel (**a**) at $D = 0$ (violet) and $D = D_c$ (orange). The black dashed and dotted lines highlight the $1/B$ dependence of the conductivity. **d** Differential conductance $G_d = dI/dV_{SD}$ as a function of the voltage bias $V_{SD}$ and magnetic field $B_\perp$ at $D = 0$. The dotted line highlights $E_g \propto B_\perp$ (see discussion in Supplementary Note 11).

by the energy $\Delta_I$ and partially layer-polarized on the bottom layer (blue), while the other pair is degenerate at two points along $k_x$ and is partially polarized on the top layer (red). Due to their partial layer polarization, the application of a displacement field shifts the two pairs of bands relative to each other based on their layer polarization. Notably, the calculations show that a band gap emerges only once the interlayer potential energy exceeds the critical value $U_c = \Delta_I/2 \approx 0.8$ meV (right panel), i.e. once $U$ counteracts the SOC, resulting in the closure of the gap between bands with the same spin (see Fig. 2e for the spin texture). This elucidates why, in the experiment, the conductivity starts decreasing with increasing displacement fields only when $D > D_c$, and associates the maxima in the conductivity with the closure of the SOC gaps. We verify this interpretation by converting $U_c$ into a displacement field, taking into account interlayer screening (see Supplementary Note 7 for details). The conversion yields a displacement field of 11.4 mV/nm, in good agreement with the experimental value of $D_c \approx 12.5$ mV/nm. Furthermore, the local conductivity minimum at $D = 0$ is observed only at low density and vanishes around $n \sim 1 \times 10^{10}$ cm$^{-2}$, which corresponds to the density required to fill the spin–orbit splitting of the bands, as demonstrated in Fig. 1f.

The local minimum in conductivity at $D = 0$ prompts consideration of a potentially insulating phase arising from the presence of a gap, as reported for BLG fully encapsulated in TMDs[14]. To verify this, we examine the temperature dependence of the conductivity in Fig. 2d. Over the temperature range of 1–10 K, the conductivity increases by one order of magnitude, indicative of insulating behavior. However, the data only conforms to the Arrhenius law within a very limited temperature range (shown in Supplementary Note 8) and saturates to rather large conductivity values at low temperatures. Similarly, the conductivity at the critical field $D_c$ also increases with temperature. Thus, although the insulating behavior is affected by the applied displacement field, it is consistently observed across all displacement fields at CN.

To further understand the temperature dependence, we compare the thermal energy $E_{th} = k_B T$ with the other characteristic energy scales determined by disorder ($E_{dis}$) and SOC ($E_{SO}$). First, we take into account the disorder potential, which induces density fluctuations of the order $\delta n \approx 2 \times 10^9$ cm$^{-2}$. These fluctuations are converted into an energy scale $E_{dis} \approx 0.14$ meV using an effective mass approximation ($m^* \approx 0.035 m_0$, where $m_0$ is the bare electron mass[36]) and taking into account the twofold valley degeneracy. At low temperatures ($E_{th} < E_{dis}$), the conductivity is governed by disorder-induced electron–hole puddles, causing the saturation of the conductivity in the temperature range labeled A in Fig. 2d. Second, the SOC introduces gaps $E_{SO} = \Delta_I/2 \approx 0.8$ meV between bands of the same spin at $D = 0$, as illustrated in Fig. 1c (see also Supplementary Note 9). The presence of these spin-resolved gaps, even without a real band gap, could explain the insulating behavior of the conductivity. Effectively, if spin is conserved in thermal activation processes, carriers cannot be thermally excited from the highest occupied valence band into the lowest unoccupied conduction band, because these bands have opposite spin. Therefore, carriers thermally excited above the spin gap $E_{SO}$ should result in an increase of conductivity with increasing temperature, which is precisely happening in the temperature range labeled B in Fig. 2d. In regime C ($E_{dis} < E_{SO} < E_{th}$), the thermal energy surpasses the SOC gap, causing the conductivity to saturate again.

Based on the results presented above, we attribute the dependence of conductivity on displacement field, density and temperature to the presence of spin–orbit-induced gaps in the spin-polarized bands in the absence of a global band gap.

### (B, D) phase diagram

In the final section of this work, we describe magnetotransport measurements at CN. Figure 3a illustrates the longitudinal conductivity $\sigma_{xx}$ as a function of the out-of-plane magnetic field ($B_\perp$) and displacement field at a temperature of $T \approx 30$ mK. With the exception of the low magnetic field peaks at $D_c$, which we discuss below, the phase diagram depicted in Fig. 3a bears a resemblance to that of pristine BLG[37,38]. Drawing on previous studies[37,39], we partition the parameter space into three distinct regions.

Phases (I) and (II), occurring at large displacement and magnetic fields, respectively, are anticipated to mirror the behavior of the BLG system in the absence of SOC. This is attributed to the dominance of energy scales dictated by the externally applied parameters ($B_\perp$ and $D$) over the SOC gap $\Delta_I/2$. Hence, we attribute phase (I) to the layer-polarized insulating state arising from the band gap induced by the displacement field, as illustrated in Fig. 2c. Phase (II) represents the insulating state of the quantum Hall $\nu = 0$ state. In this phase, our bias spectroscopy measurements uncover the presence of a gap $E_g \propto B_\perp$ (Fig. 3d), which qualitatively explains the observed $B_\perp^{-1}$ suppression of the conductivity (see dotted and dashed lines in Fig. 3c). This behavior aligns with the canted antiferromagnetic phase observed in pristine BLG[40]. Moreover, the boundaries between Phase (I) and (II) (indicated by white dotted lines and elaborated in detail in Supplementary Note 10) exhibit common characteristics with those observed in pristine BLG: the insulator-insulator transition features enhanced conductance[39,41], and the displacement field required to induce the transition is $D^*(B) \propto 2e^2B/h$[37,40,42,43].

Phase (III), emerging at $B = 0$ and $D = 0$, is expected to differ from BLG samples not in proximity with a TMD layer, due to the dominant SOC energy scale. Interestingly, a similar phase has been observed by Seiler et al.[44] in BLG/$WSe_2$ heterostructures and by Island et al.[14] in $WSe_2$/BLG/$WSe_2$. In these cases, the insulating phase was attributed to

a band gap induced either by electron correlations or SOC, respectively. Initially, the thermal activation in Phase (III) seems to support the presence of a gap. However, the temperature dependence can be explained by spin–orbit gaps in spin-polarized bands without a global band gap, as we have discussed above. In fact, while a clear gap is observed at finite magnetic fields, no gap is present at $B = 0$ (Fig. 3d), ruling out the existence of a global gap.

Now, we examine the sharp magnetoconductivity peaks at $D_c$ (see an orange curve in Fig. 3c), a novel feature of spin–orbit proximitized BLG not previously reported. With current theoretical models unable to fully explain these peaks, we explore various possibilities.

At first glance, the sharp peak in the orange curve in Fig. 3c resembles the signature of WAL, expected in materials with strong SOC. This effect has been observed in numerous transport experiments in SOC-proximitized graphene[13,25,29,30,45–47]. However, with a mean-free-path exceeding 1 µm at finite density, the condition $\ell_\phi > \ell_e$ (where $\ell_\phi$ and $\ell_e$ represent the phase-coherence length and mean-free-path, respectively) required to observe this effect would never be fulfilled ($\ell_\phi \leq 360$ nm if fitting the peak with a WAL model, as detailed in the Supplementary Note 12). Furthermore, the magnitude of the peak (~$3-4e^2/h$) exceeds what would be expected for WAL, which typically reaches up to $0.5e^2/h$ per conducting channel. Additionally, quantum interference effects are typically suppressed with increasing temperature due to the decrease in $\ell_\phi$. In contrast, the magnitude of the peak in $\sigma_{xx}$ remains robust against temperature changes (see Supplementary Note 12). For these reasons, we conclude that the peaks cannot arise from WAL.

Typically, distinguishing between how a magnetic field affects orbital or spin degrees of freedom involves tilting the field with respect to the plane. Orbital effects couple exclusively to $B_\perp$, while spin couples to $|B|$. In Fig. 3b, we compare the conductivity at $B_\perp = 0$ for $B_\parallel = 0$ and $B_\parallel = 1.8$ T (the maximum available in our system), where no significant effect is observed on $\sigma_{xx}$. The lack of an in-plane magnetic field dependence is consistent with the presence of Ising SOC, which is expected to align spins out-of-plane. Therefore, for an in-plane magnetic field dependence in conductivity to occur, the Zeeman energy $\Delta E_Z = 2\mu_B|B|$ would need to become comparable to the spin–orbit gap $\Delta_I/2$, estimated to occur at $B > 6.7$ T. In our experiments, the conductivity drops by nearly a factor of 2 at $B_\perp \approx 50$ mT. This magnetic field corresponds to a Zeeman energy of only 6 µeV, much smaller than the disorder. Therefore, it is unlikely that the Zeeman effect could be responsible for the observed magnetoconductivity peaks.

Since we could not find a suitable theoretical model relying solely on free-electron physics, we speculate that the non-monotonic magnetic field dependence of the conductivity at $D = \pm D_c$ (Fig. 3c) originates from many-body effects at CN. Electron interactions, which are strong near CN due to the lack of screening, were predicted to drive instability towards an excitonic insulator phase, in which carriers in valleys $K_+$ and $K_-$ display strong particle–hole correlations[48–52]. Previous measurements, while reporting some promising results on gap opening at CN[39,53], were not conclusive. This could be due to, among other reasons, a reduction in exchange interactions in the valley sector in the presence of spin degeneracy. In the present system, with spin degrees of freedom polarized by the SOC, carrier exchange responsible for the many-body physics at CN is expected to become stronger.

Taking this as a starting point and assuming a correlated excitonic order at CN similar to that occurring in quantum Hall bilayers (here represented by the $K_+$ and $K_-$ valleys), we interpret the nonmonotonic behavior seen in Fig. 3c as a transition between a valley-coherent order and a valley polarized order. Formally this transition is analogous to the transition between excitonic layer-coherent and layer-polarized phases investigated in quantum Hall bilayers[54]. Here it is driven by two competing mechanisms. On the one hand, the magnetic field interacts with the orbital magnetic moments arising from the Berry curvature[55]. The energy related to these orbital magnetic moments in a magnetic field is $\Delta E_M(\xi) = -\mathbf{M}\cdot\mathbf{B} = \xi g_v^* \mu_B B$, where $g_v^*$ is an effective valley $g$-factor, and $\xi = \pm 1$ is the valley index[56,57]. In nanostructures, the valley $g$-factor has been reported to range from ~10 to above 100, depending on the confinement potential[58], thus significantly larger than the usual spin Zeeman energy. This valley-dependent energy shift leads to the lifting of the valley degeneracy, favoring a valley-polarized state. On the other hand, valley polarization is associated with layer polarization once Landau levels form, introducing an energy cost for the polarization known as the capacitor-like Hartree energy[37,38,43]:

$$E_H(B) = \frac{1}{4\pi\varepsilon_0\varepsilon_{BLG}}\frac{2e^2c_0}{\ell_B^2}, \quad (2)$$

where $\varepsilon_{BLG}$ is the dielectric constant of BLG and $c_0$ is the distance between the two graphene layers. This energy counteracts the magnetization energy, thus promoting valley-unpolarized states. These mechanisms compete with each other and might contribute to the observed non-monotonic behavior in the conductivity as a function of the magnetic field.

## Discussion

In this study, we demonstrated that two types of SOC are present in spin–orbit proximitized BLG. Despite the similar magnitudes of the two SOC terms, the band splitting at zero displacement field shows little dependence on the total density, indicating that the Ising SOC predominantly influences the splitting within the density range under investigation. Our results align with previous observations of Ising superconductivity in $WSe_2$/BLG heterostructures[15,16], suggesting the potential for similar phenomena to occur in $MoS_2$/BLG systems.

Furthermore, we observed an insulating phase at $D = 0$, leading to a non-monotonic electrical conductivity with respect to the displacement field. Insulating phases with a similar displacement field dependence have been also observed in charge neutral suspended BLG[39], albeit with an intrinsic SOC two orders of magnitude weaker than in our sample[9,59]. While suspended BLG exhibits a gap at $B = 0$ and $D = 0$[53], attributed to many-body correlations, our sample does not show this behavior (Fig. 3d), suggesting a different underlying mechanism. The absence of such correlated phases in hBN-encapsulated Bernal BLG suggests that dielectric and gate screening effects may reduce the relevance of correlation phenomena. Thus, we conclude that SOC plays a crucial role in the emergence of the observed insulating phase at $D = 0$. This assertion aligns with findings by Island et al.[14], who reported a comparable insulating phase in BLG fully encapsulated in $WSe_2$. While their explanation relied on SOC-driven band inversion, our observations suggest an alternative explanation, specifically single-particle SOC-induced gaps in spin-polarized bands in the absence of a global band gap (Fig. 1e). Our conclusion is supported by a detailed analysis of the SOC strength, a comparison between the band structure calculations and the displacement field dependence, as well as temperature-dependent measurements.

While the zero magnetic field data are understood in terms of single-particle physics, we could not find a suitable theoretical model to describe the data at the finite magnetic field. We speculate that the non-monotonic magnetic field dependence of $\sigma_{xx}$ at $D = \pm D_c$ originates from many-body effects at CN. If this interpretation holds true, the system described here could serve as a platform to explore various intriguing effects anticipated for excitonic phases, such as vortices, merons, and the Josephson effect for charge-neutral particles.

*Note from the authors*. While preparing our manuscript, we became aware of a related study by Seiler et al.[44], who investigated the interplay between SOC and Coulomb interaction in $WSe_2$/BLG heterostructures, drawing conclusions on the phase diagram of SOC-proximitized BLG. It is remarkable that very similar data was obtained by two different groups, using a different TMD on bilayer graphene ($MoS_2$ by our research group and $WSe_2$ by Seiler et al.). While we

attribute this observation to a single-particle effect (spin–orbit gaps in the spin-polarized bands), Seiler et al. offer a different interpretation based on electron-electron correlations.

## Methods

### Sample fabrication

We initiate the fabrication of our devices by assembling the heterostructure using a polymer-based dry transfer technique. Each layer is obtained through mechanical exfoliation of bulk crystals onto silicon/silicon dioxide wafers. The heterostructure comprises, from top to bottom, hBN, bilayer graphene (BLG), three layers of $MoS_2$, hBN, and graphite.

The relative alignment of BLG with the $MoS_2$ layer is known to influence the strength of the SOC[20,21]. While the maximum induced SOC is anticipated around 15°–20°, the SOC is most stable against small uncontrolled twist angle variations at 0°, ensuring better reproducibility. Therefore, during the fabrication process, we carefully align the edges of the $MoS_2$ and BLG flakes, resulting in potential relative alignments of 0° or 30°. At 30°, the SOC proximity is expected to vanish, leading us to conclude that the relative angle in our sample is 0°.

Subsequently, the sample undergoes annealing in a hydro-argon atmosphere ($H_2$/Ar:5%/95%) at 350 °C for 4 h to remove polymer residues and enhance adhesion between the layers. The metallic top gate is defined using standard electron-beam lithography, followed by electron-beam evaporation (chromium/gold) and lift-off processes. The mesa is dry-etched using a reactive ion etching process with a $CHF_3$:$O_2$ mixture (40:4).

In the final fabrication step, metallic edge contacts are deposited using electron-beam lithography, followed by electron-beam evaporation (chromium/gold) and lift-off processes. After resisting development, we clean the contact area using an $O_2$ reactive ion etching process before metal deposition. This ensures the resulting contacts are ohmic and low resistive (<1 kΩ).

### Dual-gated device

We employ a dual gate structure that allows for independent tuning of the charge carrier densities $n$ and displacement field $D$. The density is defined as

$$n = \frac{1}{e}\left(C_B V_{BG} + C_T V_{TG}\right) + n_0, \tag{3}$$

and the displacement field is defined as

$$D = \frac{1}{2}\left(C_B V_{BG} - C_T V_{TG}\right) + D_0, \tag{4}$$

where $C_B = 36.7$ nF/cm$^2$ and $C_T = 78.2$ nF/cm$^2$ are the capacitance per area of the bottom and top gate, $V_{BG}$ and $V_{TG}$ are the voltages applied to the bottom and top gate. Additionally, $n_0 = -6.3E10$ cm$^{-2}$ and $D_0/\varepsilon_0 = -46$ mV/nm are offsets in the density and displacement field, respectively. These offsets are taken into account to compensate for the asymmetries arising from factors such as the contact potential difference between hBN and $MoS_2$[17].

### Measurements

The measurements were performed in a pumped Helium-4 cryostat (for temperatures above 1 K) or in a dilution refrigerator with a base temperature < 10 mK (estimated electronic temperature ≈ 30 mK).

The four-terminal resistance was measured with constant input current, by using a series resistor of 10 or 100 MΩ, depending on the resistance of the sample. The input voltage was generated at a frequency of roughly 31 Hz with a Lock-in amplifier. The current amplitude ranged from 1 to 50 nA.

**Table 1 | Values of the Slonczewski–Weiss–McClure (SWM) parameters in electron-Volt (eV)**

| SWM parameters | $\gamma_0$ | $\gamma_1$ | $\gamma_3$ | $\gamma_4$ | $\Delta$ |
|---|---|---|---|---|---|
| Exp.[60] | 3.0 | 0.40 | 0.3 | 0.15 | 0.018 |
| Th.[61] | 2.61 | 0.361 | 0.283 | 0.138 | 0.015 |

The experimental values are obtained from fits to infrared data (ref. 60). The second row provides the theoretical parameters obtained by ab initio calculations based on local density approximation (LDA)[61]. In this work, we use the experimental values to calculate the band structure.

The bias spectroscopy measurements were done in a two-terminal setup, where a DC voltage source was employed to generate the source–drain bias and a home-made voltage-to-current converter was used to detect the source–drain current.

### Tight-binding model

To determine the band structure, we employ a four-band effective tight-binding model for BLG in the basis ($A_1$, $B_1$, $A_2$, $B_2$), where $A$, $B$ are the two atoms in the unit cell of a single graphene layer, and their index represents the layer number[36]:

$$H_0 = \begin{pmatrix} -U/2 & v_0\pi^\dagger & -v_4\pi^\dagger & v_3\pi \\ v_0\pi & -U/2+\Delta & \gamma_1 & -v_4\pi^\dagger \\ -v_4\pi & \gamma_1 & U/2+\Delta & v_0\pi^\dagger \\ v_3\pi^\dagger & -v_4\pi & v_0\pi & U/2 \end{pmatrix}, \tag{5}$$

where $\pi = \hbar(\xi k_x + ik_y)$, $\pi^\dagger = \hbar(\xi k_x - ik_y)$, $U$ is the inter-layer potential energy difference, $\Delta$ is an energy difference between dimer and non-dimer atoms, and $v_j = \frac{\sqrt{3}a}{2\hbar}\gamma_j$. The parameters $\gamma_j$ are the Slonczewski–Weiss–McClure (SWM) parameters given in the "Methods" section (Table 1).

We include the extrinsic SOC given by Eq. (1). The SOC lifts the spin degeneracy but does not mix states from different $K$-valleys. Therefore, the Hamiltonian becomes an $8\times8$ matrix with the basis ($A_1\uparrow$, $A_1\downarrow$, $B_1\uparrow$, $B_1\downarrow$, $A_2\uparrow$, $A_2\downarrow$, $B_2\uparrow$, $B_2\downarrow$). Since only layer 1 is in direct contact with the $MoS_2$ layer, the SOC is taken into account only in the top-left $4\times4$ block:

$$H_{SO} = \begin{pmatrix} H_{SO}^{L1} & 0 \\ 0 & 0 \end{pmatrix} \tag{6}$$

The Ising and Rashba SOC components lead to the following $H_{SO}^{L1}$ in matrix form:

$$\begin{pmatrix} \xi\frac{\Delta_I}{2} & 0 & 0 & -i\frac{\Delta_R(\xi-1)}{2} \\ 0 & -\xi\frac{\Delta_I}{2} & i\frac{\Delta_R(\xi+1)}{2} & 0 \\ 0 & -i\frac{\Delta_R(\xi+1)}{2} & \xi\frac{\Delta_I}{2} & 0 \\ i\frac{\Delta_R(\xi-1)}{2} & 0 & 0 & -\xi\frac{\Delta_I}{2} \end{pmatrix}. \tag{7}$$

In the ordered basis ($A_1\uparrow$, $A_1\downarrow$, $B_1\uparrow$, $B_1\downarrow$, $A_2\uparrow$, $A_2\downarrow$, $B_2\uparrow$, $B_2\downarrow$), the full Hamiltonian takes the form:

$$H = H_0 + H_{SO} = \begin{pmatrix} \frac{\Delta_I\xi}{2}-\frac{U}{2} & 0 & v_0\pi^\dagger & -i\frac{\Delta_R(\xi-1)}{2} & -v_4\pi^\dagger & 0 & v_3\pi & 0 \\ 0 & -\frac{\Delta_I\xi}{2}-\frac{U}{2} & i\frac{\Delta_R(\xi+1)}{2} & v_0\pi^\dagger & 0 & -v_4\pi^\dagger & 0 & v_3\pi \\ v_0\pi & -i\frac{\Delta_R(\xi+1)}{2} & \Delta+\frac{\Delta_I\xi}{2}-\frac{U}{2} & 0 & \gamma_1 & 0 & -v_4\pi^\dagger & 0 \\ i\frac{\Delta_R(\xi-1)}{2} & v_0\pi & 0 & \Delta-\frac{\Delta_I\xi}{2}-\frac{U}{2} & 0 & \gamma_1 & 0 & -v_4\pi^\dagger \\ -v_4\pi & 0 & \gamma_1 & 0 & \Delta+\frac{U}{2} & 0 & v_0\pi^\dagger & 0 \\ 0 & -v_4\pi & 0 & \gamma_1 & 0 & \Delta+\frac{U}{2} & 0 & v_0\pi^\dagger \\ v_3\pi^\dagger & 0 & -v_4\pi & 0 & v_0\pi & 0 & \frac{U}{2} & 0 \\ 0 & v_3\pi^\dagger & 0 & -v_4\pi & 0 & v_0\pi & 0 & \frac{U}{2} \end{pmatrix}. \tag{8}$$

**Bands and density of states.** The bands are then obtained by numerically diagonalizing $H = H_0 + H_{SO}$. Each band is characterized by a band index $m$, which labels the bands from the most negative ($m = 0$) to the most positive ($m = 7$) energies.

The density of states of band $m$ is given by

$$\mathcal{D}_m(E) = \frac{1}{A}\sum_{\xi,\mathbf{k}} \delta(E - E_{m\xi,\mathbf{k}}) \tag{9}$$

where $\xi$ is the valley quantum number, and $\mathbf{k}$ is the wave vector. $A = L^2$ is the area in real space. The delta function is approximated by a Gaussian function

$$\delta(E - E_{m,\xi,\mathbf{k}}) \approx \frac{1}{\sqrt{2\pi}\epsilon}\exp\left(-\frac{(E - E_{m,\xi,\mathbf{k}})^2}{2\epsilon^2}\right), \tag{10}$$

with an energy broadening of $\epsilon < 50\,\mu\text{eV}$. The band structure $E_{m,\xi,\mathbf{k}}$ is calculated on a grid in $k$ space with finite resolution $\Delta k \sim 1 \times 10^5\,\text{m}^{-1}$. Therefore the sum needs to be renormalized by the factor

$$\left(\frac{\Delta k}{2\pi/L}\right)^2. \tag{11}$$

Equations (9), (10) and (11) yield the density of states of band $m$:

$$\mathcal{D}_m(E) = \left(\frac{\Delta k}{2\pi}\right)^2 \sum_{\xi,\mathbf{k}} \frac{1}{\sqrt{2\pi}\epsilon}\exp\left(-\frac{(E - E_{m,\xi,\mathbf{k}})^2}{2\epsilon^2}\right). \tag{12}$$

The total density of states is obtained by summing over the band index $m$.

The electron density is obtained by integrating over the conduction band ($m \geq 4$), while the hole density is obtained by integrating over the valence band ($m < 4$)

$$\begin{aligned} n_e(E_F) &= \sum_{m=4}^{7} \int_{-\infty}^{E_F} \mathcal{D}_m(E)\mathrm{d}E \\ n_h(E_F) &= \sum_{m=0}^{3} \int_{\infty}^{E_F} \mathcal{D}_m(E)\mathrm{d}E. \end{aligned} \tag{13}$$

Out of the 8 bands, we only consider the four low energy bands ($2 \leq m \leq 5$), $m = 4$, 5 for the conduction band and $m = 2$, 3 for the valence band. The total density is obtained by summation:

$$n(E_F) = n_e(E_F) - n_h(E_F). \tag{14}$$

According to our definition, hole doping corresponds to a negative density.

## Data availability

Source data and analysis scripts generated in this study have been deposited in the ETH Research Collection under accession code https://doi.org/10.3929/ethz-b-000662935.

## References


1. Burkard, G., Ladd, T. D., Pan, A., Nichol, J. M. & Petta, J. R. Semiconductor spin qubits. *Rev. Mod. Phys.* **95**, 025003 (2023).
2. Rashba, E. I. & Efros, A. L. Orbital mechanisms of electron-spin manipulation by an electric field. *Phys. Rev. Lett.* **91**, 126405 (2003).
3. Khoo, J. Y., Morpurgo, A. F. & Levitov, L. On-demand spin-orbit interaction from which-layer tunability in bilayer graphene. *Nano Lett.* **17**, 7003–7008 (2017).
4. Avsar, A. et al. Colloquium: spintronics in graphene and other two-dimensional materials. *Rev. Mod. Phys.* **92**, 021003 (2020).
5. Trauzettel, B., Bulaev, D. V., Loss, D. & Burkard, G. Spin qubits in graphene quantum dots. *Nat. Phys.* **3**, 192–196 (2007).
6. Gächter, L. M. et al. Single-shot spin readout in graphene quantum dots. *PRX Quantum* **3**, 020343 (2022).
7. Garreis, R. et al. Long-lived valley states in bilayer graphene quantum dots. *Nat. Phys.* 1–7 (2024). https://www.nature.com/articles/s41567-023-02334-7.
8. Denisov, A. O. et al. Ultra-long relaxation of a Kramers qubit formed in a bilayer graphene quantum dot. Preprint at http://arxiv.org/abs/2403.08143 (2024).
9. Kane, C. L. & Mele, E. J. Quantum spin hall effect in graphene. *Phys. Rev. Lett.* **95**, 226801 (2005).
10. Sichau, J. et al. Resonance microwave measurements of an intrinsic spin–orbit coupling gap in graphene: a possible indication of a topological state. *Phys. Rev. Lett.* **122**, 046403 (2019).
11. Duprez, H. et al. Spectroscopy of a single-carrier bilayer graphene quantum dot from time-resolved charge detection. Preprint at http://arxiv.org/abs/2311.12949 (2023).
12. Avsar, A. et al. Spin-orbit proximity effect in graphene. *Nat. Commun.* **5**, 4875 (2014).
13. Wang, Z. et al. Origin and magnitude of 'designer' spin–orbit interaction in graphene on semiconducting transition metal dichalcogenides. *Phys. Rev. X* **6**, 041020 (2016).
14. Island, J. O. et al. Spin–orbit-driven band inversion in bilayer graphene by the van der Waals proximity effect. *Nature* **571**, 85–89 (2019).
15. Zhang, Y. et al. Enhanced superconductivity in spin-orbit proximitized bilayer graphene. *Nature* **613**, 268–273 (2023).
16. Holleis, L. et al. Ising superconductivity and nematicity in Bernal bilayer graphene with strong spin–orbit coupling. Preprint at http://arxiv.org/abs/2303.00742 (2023).
17. Gmitra, M. & Fabian, J. Proximity effects in bilayer graphene on monolayer $WSe_2$: field-effect spin valley locking, spin–orbit valve, and spin transistor. *Phys. Rev. Lett.* **119**, 146401 (2017).
18. Rashba, E. I. Graphene with structure-induced spin–orbit coupling: spin-polarized states, spin zero modes, and quantum hall effect. *Phys. Rev. B* **79**, 161409 (2009).
19. Khoo, J. Y. & Levitov, L. Tunable quantum Hall edge conduction in bilayer graphene through spin–orbit interaction. *Phys. Rev. B* **98**, 115307 (2018).
20. Li, Y. & Koshino, M. Twist-angle dependence of the proximity spin-orbit coupling in graphene on transition-metal dichalcogenides. *Phys. Rev. B* **99**, 075438 (2019).
21. David, A., Rakyta, P., Kormányos, A. & Burkard, G. Induced spin–orbit coupling in twisted graphene–transition metal dichalcogenide heterobilayers: Twistronics meets spintronics. *Phys. Rev. B* **100**, 085412 (2019).
22. Naimer, T., Zollner, K., Gmitra, M. & Fabian, J. Twist-angle dependent proximity induced spin–orbit coupling in graphene/transition metal dichalcogenide heterostructures. *Phys. Rev. B* **104**, 195156 (2021).
23. Chou, Y.-Z., Wu, F. & Das Sarma, S. Enhanced superconductivity through virtual tunneling in Bernal bilayer graphene coupled to $WSe_2$. *Phys. Rev. B* **106**, L180502 (2022).
24. Yang, B. et al. Strong electron-hole symmetric Rashba spin–orbit coupling in graphene/monolayer transition metal dichalcogenide heterostructures. *Phys. Rev. B* **96**, 041409 (2017).
25. Zihlmann, S. et al. Large spin relaxation anisotropy and valley-Zeeman spin–orbit coupling in $WSe_2$/graphene/*h*-BN heterostructures. *Phys. Rev. B* **97**, 075434 (2018).
26. Wang, D. et al. Quantum Hall effect measurement of spin-orbit coupling strengths in ultraclean bilayer graphene/$WSe_2$ heterostructures. *Nano Lett.* **19**, 7028–7034 (2019).
27. Ingla-Aynés, J., Herling, F., Fabian, J., Hueso, L. E. & Casanova, F. Electrical control of valley-zeeman spin–orbit-coupling–induced spin precession at room temperature. *Phys. Rev. Lett.* **127**, 047202 (2021).
28. Sun, L. et al. Determining spin–orbit coupling in graphene by quasiparticle interference imaging. *Nat. Commun.* **14**, 3771 (2023).

29. Wang, Z. et al. Strong interface-induced spin–orbit interaction in graphene on $WS_2$. *Nat. Commun.* **6**, 8339 (2015).
30. Wakamura, T. et al. Spin–orbit interaction induced in graphene by transition metal dichalcogenides. *Phys. Rev. B* **99**, 245402 (2019).
31. Fülöp, B. et al. Boosting proximity spin–orbit coupling in graphene/WSe2 heterostructures via hydrostatic pressure. *npj 2D Mater. Appl.* **5**, (2021). https://www.nature.com/articles/s41699-021-00262-9.
32. Benítez, L. A. et al. Tunable room-temperature spin galvanic and spin hall effects in van der Waals heterostructures. *Nat. Mater.* **19**, 170–175 (2020).
33. Bergemann, C. Fermi surface measurements. In *Encyclopedia of Condensed Matter Physics* (eds Bassani, F., Liedl, G. L. & Wyder, P.) 185–192 (Elsevier, 2005).
34. Rhodes, D., Chae, S. H., Ribeiro-Palau, R. & Hone, J. Disorder in van der Waals heterostructures of 2d materials. *Nat. Mater.* **18**, 541–549 (2019).
35. Yankowitz, M., Ma, Q., Jarillo-Herrero, P. & LeRoy, B. J. van der Waals heterostructures combining graphene and hexagonal boron nitride. *Nat. Rev. Phys.* **1**, 112–125 (2019).
36. McCann, E. & Koshino, M. The electronic properties of bilayer graphene. *Rep. Prog. Phys.* **76**, 056503 (2013).
37. Nandkishore, R. & Levitov, L. Spontaneously ordered states in bilayer graphene. *Phys. Scr.* **2012**, 014011 (2012)
38. Knothe, A. & Jolicoeur, T. Phase diagram of a graphene bilayer in the zero-energy Landau level. *Phys. Rev. B* **94**, 235149 (2016).
39. Weitz, R. T., Allen, M. T., Feldman, B. E., Martin, J. & Yacoby, A. Broken-symmetry states in doubly gated suspended bilayer graphene. *Science* **330**, 812–816 (2010).
40. Kharitonov, M. Antiferromagnetic state in bilayer graphene. *Phys. Rev. B* **86**, 195435 (2012).
41. Maher, P. et al. Evidence for a spin phase transition at charge neutrality in bilayer graphene. *Nat. Phys.* **9**, 154–158 (2013).
42. Gorbar, E. V., Gusynin, V. P. & Miransky, V. A. Energy gaps at neutrality point in bilayer graphene in a magnetic field. *JETP Lett.* **91**, 314–318 (2010).
43. Tőke, C. & Fal'ko, V. I. Intra-landau-level magnetoexcitons and the transition between quantum hall states in undoped bilayer graphene. *Phys. Rev. B* **83**, 115455 (2011).
44. Seiler, A. M. et al. Layer-selective spin–orbit coupling and strong correlation in bilayer graphene. Preprint at http://arxiv.org/abs/2403.17140 (2024).
45. Wakamura, T. et al. Strong anisotropic spin–orbit interaction induced in graphene by monolayer $ws_2$. *Phys. Rev. Lett.* **120**, 106802 (2018).
46. Tiwari, P., Srivastav, S. K. & Bid, A. Electric-field-tunable valley Zeeman effect in bilayer graphene heterostructures: realization of the spin–orbit valve effect. *Phys. Rev. Lett.* **126**, 096801 (2021).
47. Amann, J. et al. Counterintuitive gate dependence of weak antilocalization in bilayer graphene/$WSe_2$ heterostructures. *Phys. Rev. B* **105**, 115425 (2022).
48. Kharitonov, M. Y. & Efetov, K. B. Electron screening and excitonic condensation in double-layer graphene systems. *Phys. Rev. B* **78**, 241401 (2008).
49. Nandkishore, R. & Levitov, L. Dynamical screening and excitonic instability in bilayer graphene. *Phys. Rev. Lett.* **104**, 156803 (2010).
50. Zhang, F., Min, H., Polini, M. & MacDonald, A. H. Spontaneous inversion symmetry breaking in graphene bilayers. *Phys. Rev. B* **81**, 041402 (2010).
51. Kharitonov, M. Y. & Efetov, K. B. Excitonic condensation in a double-layer graphene system. *Semicond. Sci. Technol.* **25**, 034004 (2010).
52. Throckmorton, R. E. & Das Sarma, S. Quantum multicriticality in bilayer graphene with a tunable energy gap. *Phys. Rev. B* **90**, 205407 (2014).
53. Velasco, J. et al. Transport spectroscopy of symmetry-broken insulating states in bilayer graphene. *Nat. Nanotechnol.* **7**, 156–160 (2012).
54. Eisenstein, J. Exciton condensation in bilayer quantum hall systems. *Annu. Rev. Condens. Matter Phys.* **5**, 159–181 (2014).
55. Xiao, D., Chang, M.-C. & Niu, Q. Berry phase effects on electronic properties. *Rev. Mod. Phys.* **82**, 1959–2007 (2010).
56. Overweg, H. et al. Topologically nontrivial valley states in bilayer graphene quantum point contacts. *Phys. Rev. Lett.* **121**, 257702 (2018).
57. Banszerus, L. et al. Spin-valley coupling in single-electron bilayer graphene quantum dots. *Nat. Commun.* **12**, 5250 (2021).
58. Lee, Y. et al. Tunable valley splitting due to topological orbital magnetic moment in bilayer graphene quantum point contacts. *Phys. Rev. Lett.* **124**, 126802 (2020).
59. Konschuh, S., Gmitra, M., Kochan, D. & Fabian, J. Theory of spin–orbit coupling in bilayer graphene. *Phys. Rev. B* **85**, 115423 (2012).
60. Zhang, L. M. et al. Determination of the electronic structure of bilayer graphene from infrared spectroscopy. *Phys. Rev. B* **78**, 235408 (2008).
61. Jung, J. & MacDonald, A. H. Accurate tight-binding models for the $\pi$ bands of bilayer graphene. *Phys. Rev. B* **89**, 035405 (2014).
62. Kharitonov, M. Canted antiferromagnetic phase of the $\nu = 0$ quantum hall state in bilayer graphene. *Phys. Rev. Lett.* **109**, 046803 (2012).


## Acknowledgements

We thank Thomas Weitz, Anna Seiler, and Patrick Lee for fruitful discussions. We thank Peter Märki, Thomas Bähler, as well as the FIRST staff for their technical support. We acknowledge support from the European Graphene Flagship Core 3 Project, the Swiss National Science Foundation via NCCR Quantum Science, and the H2020 European Research Council (ERC) Synergy Grant under Grant Agreement 95154. N.J. acknowledges funding from the International Center for Advanced Studies of Energy Conversion (ICASEC). K.W. and T.T. acknowledge support from the JSPS KAKENHI (Grant Numbers 20H00354 and 23H02052) and World Premier International Research Center Initiative (WPI), MEXT, Japan.

## Author contributions

M.M., H.D., T.I., and K.E. conceived and designed the experiments. M.M., M.G., and F.F. performed and analyzed the measurements with inputs from H.D., J.D.G., and M.N. M.M. designed the figures with inputs from C.T. and H.D. M.M. and M.G. fabricated the device with inputs from J.G., M.N., and H.D. A.P., N.J., and L.L. provided theoretical support. T.T. and K.W. supplied the hexagonal boron nitride. M.M. wrote the manuscript with inputs from H.D. All the coauthors mentioned above read and commented on the manuscript.

## Competing interests

The authors declare no competing interests.

## Additional information

**Supplementary information** The online version contains supplementary material available at https://doi.org/10.1038/s41467-024-53324-z.

**Correspondence** and requests for materials should be addressed to Michele Masseroni or Klaus Ensslin.

**Peer review information** *Nature Communications* thanks the anonymous, reviewer(s) for their contribution to the peer review of this work. A peer review file is available.